The Planetary Science Journal, 1:55 (18pp), 2020 December https://doi.org/10.3847/PSJ/abb60f

Unprecedented Molecular Diversity Revealed in Meteoritic Insoluble Organic Matter: The Paris Meteorite's Case

Grégoire Danger[1,2,3], Alexander Ruf[1], Julien Maillard[4,5,6,7], Jasmine Hertzog[8,9], Vassilissa Vinogradoff[1,2], Philippe Schmitt-Kopplin[8,9], Carlos Afonso[4,5,6], Nathalie Carrasco[7], Isabelle Schmitz-Afonso[4,5,6], Louis Le Sergeant d'Hendecourt[1,2], and Laurent Remusat[10]

[1] Laboratoire de Physique des Interactions Ioniques et Moléculaires, UMR 7345, Aix-Marseille Université, CNRS, Centre de St-Jérôme, Marseille, France
gregoire.danger@univ-amu.fr
[2] Aix Marseille Université, CNRS, CNES, LAM, Marseille, France
[3] Institut Universitaire de France (IUF), France
[4] Normandie Univ, COBRA UMR 6014 et FR 3038 Univ Rouen, France
[5] INSA Rouen, France
[6] CNRS IRCOF, 1 Rue Tesnière, F-76821 Mont-Saint-Aignan Cedex, France
[7] LATMOS/IPSL, Université Versailles St Quentin, UPMC Université Paris 06, CNRS, 11 blvd d'Alembert, F-78280 Guyancourt, France
[8] Helmholtz Zentrum München, Analytical BioGeoChemistry, Neuherberg, Germany
[9] Technische Universität München, Chair of Analytical Food Chemistry, Freising-Weihenstephan, Germany
[10] Muséum National d'Histoire Naturelle, Sorbonne Université, UMR CNRS 7590, Institut de minéralogie, de physique des matériaux et de cosmochimie, Paris, France

Received 2020 June 8; revised 2020 August 17; accepted 2020 August 26; published 2020 October 26

Abstract

The insoluble organic matter (IOM) contained in carbonaceous chondrites has witnessed a diverse suite of processes possibly starting from the evolution of the parent molecular cloud down to the protosolar nebula and finally to asteroidal processes that occurred on the chondrites' parent bodies. Laser desorption coupled with ultra-high-resolution mass spectrometry reveals that the IOM of the Paris meteorite releases a large diversity of molecules. Various molecular families ranging from hydrogenated amorphous carbon to CHNOS aromatic molecules were detected with heteroatoms (nitrogen, oxygen, and sulfur) mainly incorporated within aromatic structures. Molecules bearing nitrogen atoms present a significant variation in aromaticity. These unprecedented results allow the proposal that small molecules bearing heteroatoms could be trapped in the large macromolecular network of the IOM by hydrophobic interactions. This molecular diversity could originate from different sources, such as the soluble organic matter, the hydrothermal alteration inside the Paris's parent body, or even generated during the IOM extraction procedure. It has to be noted that some of the molecular diversity may reflect fragmentation and rearrangement of the IOM constituents during the laser desorption ionization, although care was taken to minimize such damage.

Unified Astronomy Thesaurus concepts: Meteorites (1038); Carbonaceous chondrites (200); Meteorite composition (1037); Mass spectrometry (2094)

1. Introduction

Carbonaceous chondrites (CCs) are fragments of primitive asteroids that are known to contain up to 6 wt% of organic matter (OM; Pearson et al. 2006). Insoluble organic matter (IOM) represents the major organic carbon component ofCCs (75–95 wt% of the total recovered organic matter; Sephton 2002; Pizzarello et al. 2006; Schmitt-Kopplin et al. 2010, 2012; Remusat 2015; Ruf et al. 2018). Its isotope compositions, in particular the D/H ratio, indicate that it derives from precursors possibly originating from the interstellar medium or the cold regions of the outer solar system that were subsequently accreted on the CC parent bodies (Remusat et al. 2010). Analyses reveal that the IOM is constituted of aromatic units, up to coronene (seven-ring units), with 20%–30% of aliphatic structures, mainly in the form of bridges between these structures (Gardinier et al. 2000; Cody et al. 2002; Cody & Alexander 2005; Remusat et al. 2005a; Yabuta et al. 2005; Orthous-Daunay et al. 2013), up to seven carbon atoms for the aliphatic bridges and four carbons for the side chains on the aromatic units (Remusat et al. 2005a). Heteroatoms also compose the IOM with up to 20% of oxygen and only 3% of nitrogen, roughly reflecting the cosmic abundance ratios of these two elements. Oxygen is mainly in the form of ether and ester groups (Hayatsu et al. 1977; Remusat et al. 2005a, 2005b) but also in the form of furans, contributing to the aromatic units (Cody et al. 2011). Nitrogen can occur in nitrile groups or inside heterocycles such as pyrroles (five-membered rings; Remusat et al. 2005a). The amount of sulfur is equivalent to nitrogen and is involved in thiophene structures, as well as sulfoxide and sulfone in the aliphatic chains (Remusat et al. 2005a; Orthous-Daunay et al. 2010). As a result, the IOM is schematically represented as a cross-linked structure of aromatic and aliphatic units with some heteroatoms, constituting macromolecules (Derenne & Robert 2010). This complex macromolecular assemblage would have an approximate global composition of $C_{100}H_{60-80}O_{16-18}N_3S_{2-7}$ (Alexander et al. 2007; Derenne & Robert 2010). Its condensed structure made the IOM resistant to secondary processes that occurred during the parent body evolution. Therefore, the IOM includes rare components that record the conditions that occurred during the evolution of the molecular cloud into the solar system (Remusat 2015).

We choose the Paris meteorite because it is the least aqueously altered CM chondrite reported thus far; it must be noted that the IOM of the CM chondrites has been intensively

studied over the past 30 yr, making them a case study for extraterrestrial organic macromolecules. Found in 2012, the Paris meteorite has been classified as an unmetamorphosed chondrite, 2.7–2.9 CM in the aqueous alteration scale defined by Rubin et al. (2007). Its peculiar mineralogical heterogeneities, the significant porosity, the persistence of Fe–Ni metal (usually absent in CMs), and the presence of amorphous silicates and nanosulfides in the matrix imply that the Paris CM chondrite only experienced gentle hydrothermal processing compared to other CM meteorites (Hewins et al. 2014; Marrocchi et al. 2014; Leroux et al. 2015). Previous analysis of Paris IOM revealed a lower aromatic/aliphatic carbon ratio than other CMs and a lower content of oxygen atoms (Vinogradoff et al. 2017), but globally the same macromolecular assemblages as described above.

In this contribution, we report new results obtained from laser desorption ionization (LDI) coupled to an ultra-high-resolution mass spectrometer (FT-ICR-MS) on a Paris IOM. The LDI is well suited for the analysis of IOM due to the low volatility and solubility of the involved components. With this technique, direct information is obtained on the molecular content of this Paris IOM sample by preventing as much as possible molecule degradation before their detection. The coupling of LDI with high-resolution mass spectrometry then allows information on the molecular diversity present in this IOM to be obtained. We indeed reveal new and original information on the molecular composition, diversity, and aromaticity of the Paris IOM that can be related to synthesis environments during the early ages of the solar system.

2. Methods

2.1. Isolation of the Paris IOM

The isolation of the Paris IOM is described by Vinogradoff et al. (2017) and reported hereafter. About 15 g of the Paris meteorite were provided by the Muséum National d'Histoire Naturelle, Paris, France. Matrix and chondrules were separated (Göpel et al. 2015). A matrix-enriched sample was crushed in an agate mortar, and IOM was subsequently isolated using the protocols described in Remusat et al. (2005b, 2008). In brief, the powdered matrix was subjected to several extractions in water, acetone, and dichloromethane/methanol (2:1, vol/vol). The solid residue was then subjected to HF/HCl treatment by stirring in a mixture of HF/HCl (16N/6N, 2:1, vol/vol) for 24 hr at room temperature under nitrogen flux. The residue was then washed many times with HCl (6N) for 2 hr at 70°C (i.e., to remove fluoride precipitates) until the final solute was colorless. The acid residue was then washed 10 times with water, extracted 3 times with acetone and a mixture of CH_2Cl_2/MeOH, 2:1 vol/vol, and dried under nitrogen. A residue of about 150 mg was recovered.

2.2. Paris IOM Analysis by LDI-FT-ICR-MS(/MS)

All analyses were performed in Rouen, France, on an FT-ICR Solarix XR mass spectrometer (Bruker Daltonics Germany) equipped with a 12 T superconducting magnet and an LDI source (laser NdYAg × 3 355 nm). The mass spectrometer was externally calibrated with a solution of sodium trifluoroacetate. One mg of the Paris IOM was crushed, and about 0.1 mg were deposited on a LDI plate without any additional matrix (Barrère et al. 2012). Mass spectra were obtained using the broadband mode from m/z 110.6 to m/z 1200.0 with the sum of 400 scans in positive ion mode. The analogical signal was amplified and digitalized with 16 million points, resulting in the recording of transient of 5 s, which was transformed into the corresponding frequency domain by Fourier transform (one zero fill and full sine apodization). This resulted in magnitude mode spectra with a mass resolving power (resolution) of 1.100.000 at m/z 400. No signals relative to the Paris IOM signature were detected in blanks (Appendix A.1). All spectra were phased, and the resulting absorption mode spectrum had a resolution of 2.500.000 at m/z 400 (Qi et al. 2012). The following instrumental parameters were implemented: plate offset 100 V, deflector plate 210 V, laser power 11% (0.25 μJ) or 13% (0.30 μJ), spot size 30 μm, fluence at 11% 36.7 mJ cm^{-2} and at 13% 42.26 mJ cm^{-2}, laser shots 50, laser shots frequency 1000 Hz, funnel 1 at 150 V, and skimmer 1 at 25 V. Compared to LDI-TOFMS, FT-ICR presents a higher sensitivity and resolution.

For tandem mass spectrometry experiments (MS/MS), several nominal masses were isolated in a quadrupole and then fragmented by acceleration in a collision cell filled with argon. This collision-induced dissociation (CID) allows controlled fragmentation to be achieved by adjusting the value of the imposed acceleration voltage (the higher the voltage, the greater the fragmentation). The same parameters were used for the MS and MS/MS experiments, except for the laser power that was raised to 25% of the nominal laser power (thus, 0.58 μJ), and the number of shots was increased to 200 in order to obtain a decent signal.

LDI ionization techniques are well suited for analyzing insoluble organic materials. However, a drawback of these techniques is the possibility of the organic compounds fragmenting and recombining if the laser energy is not well tuned (Aubriet et al. 2018; Wu et al. 2013). In order to avoid these phenomena, different laser powers were tested (11%, 13%, and 20%). From the achieved mass spectra profiles (see Appendix A.2), it is assumed that the 11% laser power impedes the formation of artifacts and mainly molecular ions are detected in the form of $[M+H]^+$ and $[M]^{\bullet+}$. Furthermore, a laser power lower than 11% gave the same spectral signatures but with an important sensitivity decrease, implying that 11% provides the best compromise between sensitivity and limitation of fragmentations. In optimized conditions, LDI ensures compounds are detected over a similar mass range but with different chemical properties (more aromatic) from ESI (Maillard et al. 2018). Higher-mass molecules were observed with a laser power of 13% and 20% compared to those obtained at 11%. For instance, at 11%, the energy is not sufficient to ionize fullerene or to generate them by molecular recombinations because fullerenes are not observed. Therefore, molecules detected at 11% are for a large fraction initially free and are not generated by molecular recombination or covalently bonded to the macromolecular structures.

2.3. Data Treatment

Compass DataAnalysis 5.0 software (Bruker Daltonics, Germany) was used to process the FT-ICR mass spectrum. The mass spectrum was first calibrated with a list of well-characterized ions from the hydrocarbon and fullerene (C48-74) molecular series. The mass accuracy achieved for these ions was between ±200 ppb. A peak list at signal-to-noise ratio (S/N) greater than 6 was generated, and magnetron and satellite signals were removed as previously reported (Kanawati et al. 2017). The filtered mass list was then subject to assignment by means of

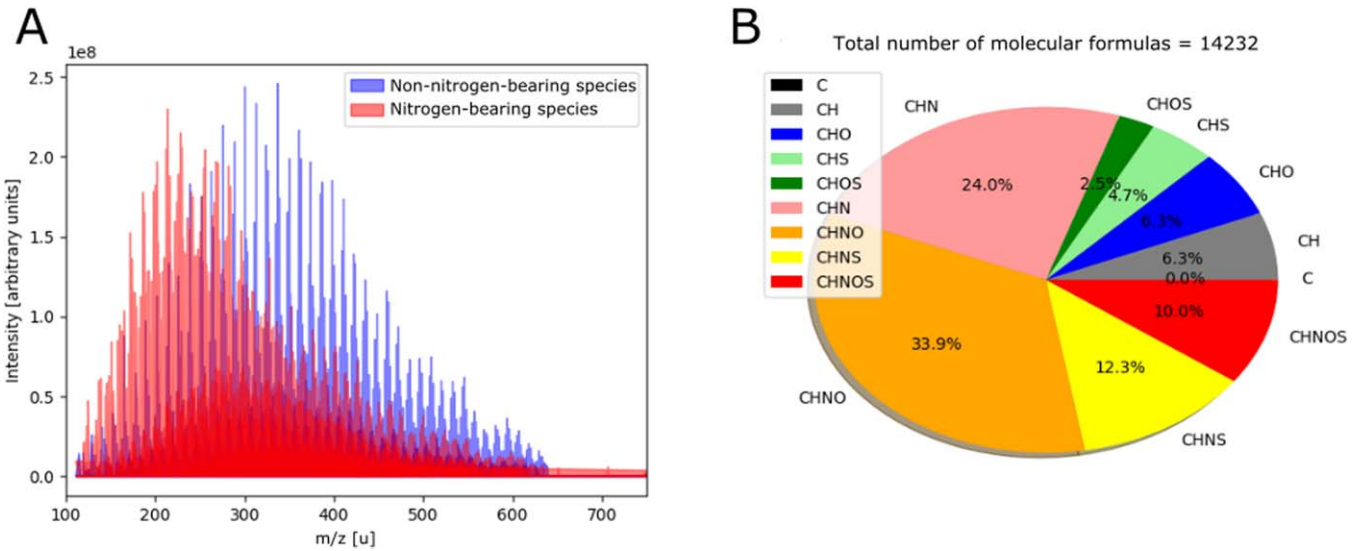

Figure 1. Distributions of nitrogen and non-nitrogen-bearing species in the LDI-FT-ICR mass spectrum (laser energy of 11%) of Paris IOM (A) and (B), partition of the 14,232 attributions in chemical families (C, CH, CHO, CHS, CHOS, CHN, CHNO, CHNS, or CHNOS).

Composer software (Sierra Analytics, Modesto, CA). Thus, both protonated and radical cations were assigned with general formulas $C_{0–200}H_{0–1000}O_{0–6}N_{0–6}S_{0–6}$ within a 0.4 ppm mass accuracy window and DBE ranging from −0.5 to 100. Error plots for assignment validation are shown in Appendix A.3 (Figure A4). Thousands of features that belong to different heteroatom classes were achieved. Further data processing was performed via Python.

Calculation of X_C. The aromaticity equivalent X_C was calculated, according to the following formula (Yassine et al. 2014): $X_C = ((2 \times n(C) + n(N) - n(H) - 2 \times m \times n(O))/(DBE - m \times n(O))) + 1$ with $DBE = n(C) - n(H)/2 + n(N)/2 + 1$, where m corresponds to an estimate of the oxygen fraction linked to carbon by double bonds; $m = 0.75$ based on NMR data (Vinogradoff et al. 2017). Chemical classes, aliphatics, aromatics, and condensed aromatics were defined accordingly: aliphatics $0 < X_c < 2.5$, aromatics (one aromatic ring, like benzene) $2.5 < X_c < 2.7$, and condensed aromatics (more aromatic rings like in PAH) $2.7 < X_c$. From these X_c values, the degree of aromaticity will be estimated based on the distribution between condensed aromatics, aromatics, and aliphatics.

3. Results

3.1. Molecular Diversity in the Paris IOM

The LDI-FT-ICR mass spectrum of the Paris IOM presents a large number of signals from which 14,232 molecular formulas were assigned (Figure 1). To obtain information on the carbon skeleton of molecules, the degree of aromaticity was estimated for each molecular formula (estimated from the aromaticity factor X_c; details in Appendix A.4, Figure A5). Condensed aromatic structures correspond to 90.9% of these attributions. Aromatic structures represent 6.9% and only 2.2% of these attributions are referred to aliphatic ones. This aromaticity description is relevant to the general view of IOM structures, which are mainly considered as highly aromatic with a few aliphatic bridges cross-linking the aromatic structures.

Among the 14,232 attributed ions, eight different chemical families could be differentiated (Figure 1(B)). Nitrogen-bearing species represent 80.2% of the molecular attributions, with the CHNO family representing 33.9% of the total formulas (Figure 1(B)). It is known that LDI privileges ionization of PAH's bearing basic functions such as nitrogen chemical groups. This difference in the number of attributed ions can thus be amplified by the ionization technique that we used (Cho et al. 2013). For non-nitrogen-bearing species, CH and CHO families are the most abundant ones, with 6.3% of the total attributions for each. In Figure 1(A), the mass spectrum also presents separately the mass distributions related to nitrogen-bearing attributions (in red) and non-nitrogen-bearing species (in blue). While the non-nitrogen-bearing families do present a homogenous maximum in peak intensity at 330 u, two different mass distributions are clearly distinguishable among the nitrogen-bearing species (see also Appendix A.5, Figure A6). When the number of heteroatoms increases (O, S, or O+S), the maximum varies from 230 u for CHN to 330 u for CHNOS.

These chemical families can be displayed using DBE (double bond equivalent) versus number of carbons (#C) plots, highlighting the different distributions (Figure 2(A)). The non-nitrogen-bearing families present a homogenous trend near the PAH lines, implying that these molecules are mainly polycondensed aromatic structures. The evaluation of the degree of aromaticity (via X_c) presents condensed structures at 97% for the non-nitrogen-bearing attributions (Figure 2(B)), with a number of hydrogen atoms more than half times lower than the number of carbon (Appendix A.5).

Compared to the non-nitrogen-bearing species, nitrogen-bearing ones present two different distributions, divided into zones 1 and 2 (Figures 2(B) and A7(A)), relative to the non-N-bearing species. One observes a similar trend to the non-nitrogen-bearing families (zone 1), while the second represents lower DBE values suggesting a lower degree of aromaticity (Appendix A.5). This is confirmed by the degree of aromaticity where zone 1 is similar to the non-nitrogen-bearing species, while zone 2 presents lower amounts of condensed aromatics and higher amounts of aromatic and aliphatic structures (Figure 2(B)). By separating the nitrogen-bearing families into these two zones, we observe that zone 1 follows the PAH line of the non-nitrogen-bearing families, with a similar H/C

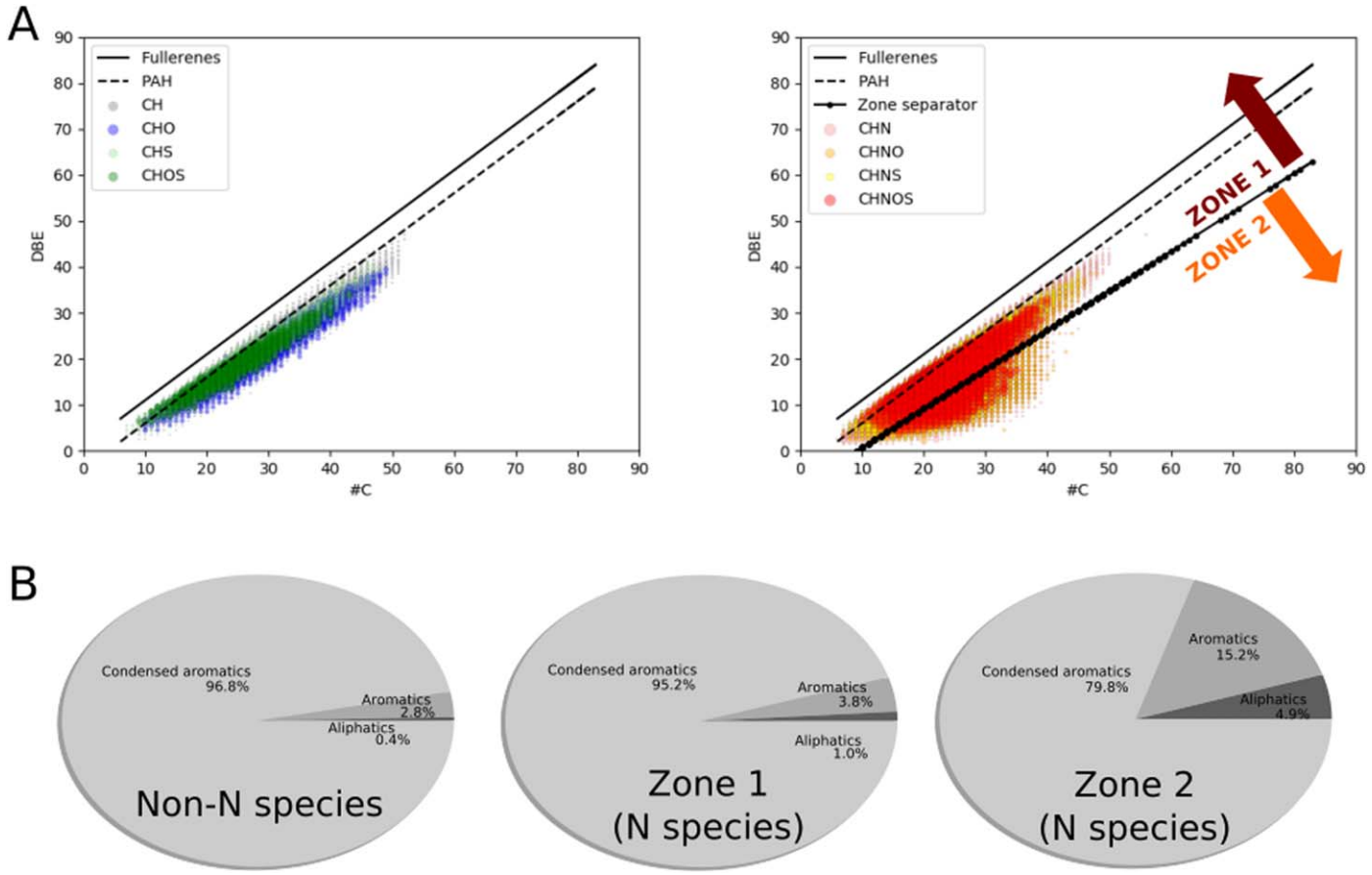

Figure 2. Double bond equivalent (DBE) vs. the number of carbon (#C) for each molecular formula is plotted, with the dotted line indicating the PAH trend, the full line indicating fullerene composition and a separator line between both distributions observed for nitrogen-bearing species (A). X_c pie chart of the three distinct distributions, showing the proportions of condensed aromatic, aromatic, and aliphatic structures (B). Laser energy at 11% of the laser power.

atomic ratio (~0.6). Zone 2 however, presents lower DBE/#C ratios and a much higher H/C (1.2), implying species containing the lowest number of condensed aromatic structures (79.8%) and the highest number of aliphatic structures (4.9%). Zone 1 and zone 2 hence present different molecular carbon skeletons. Nonetheless, each zone contains the same number of O and N relative to carbon, with only weaker amounts of S relative to C for zone 2 (Appendix A.5).

3.2. Higher-mass Molecular Content and Pure Carbon Structures

We tested for the presence of PAH-like structures in the Paris IOM by varying the laser power between 11%, 13%, and 20% (Santos et al. 2016; Wang et al. 2020). The laser power corresponds to the amount of energy that impacts the sample to obtain the desorption and ionization of molecules. It has to be noted that depending on the laser energy, secondary reactions such as pyrolysis and molecular recombination could occur. Consequently, it is important to carefully evaluate the impact of the laser power percentage as described in Appendix A.2 that estimate at 11% the energy limiting these recombinations. With the 13% laser power analysis, the number of attributions increases from 14,232 to 21,881 (Figure 3(A)), potentially reflecting the thermal heating effect generated by the laser spot, which then allows for the desorption of new species with lower net vapor pressure. Furthermore, the family distribution is directly impacted (Figure 3(A)). Nitrogen-bearing families are still the most abundant but their relative percentage drops to 68.6%. This is clearly due to an increase in the number of non-nitrogen-bearing attributions. CHOS and CHS especially do increase to 7.0% (versus 2.5%) and 7.3% (versus 4.7%), respectively, of the total attributions. Furthermore, some pure carbon structures do appear and represent 0.2%. This increase in the number of non-nitrogen-bearing species at higher laser power could imply that these species represent large condensed structures presenting higher desorption energies (Appendix A.6, Figure A8 and A9).

DBE versus #C for attributions at the 13% laser power analysis (Figure 3(B)) shows that for higher laser power, the number of attributions presenting a higher DBE increases for the same carbon number. Indeed, a higher number of attributions is observed between PAHs and pure carbon lines, confirming an increase of the degree of aromaticity of the detected ions (H/C = 0.81 for 11% versus H/C = 0.60 for 13%). The combination of analyses at 11% and 13% laser power shows a significant molecular diversity in the Paris IOM in terms of the number of released molecules but also in their degree of aromaticity. Indeed, higher masses of species containing up to 90 carbons are also detected, with the presence of fullerene-like structures and particularly the C_{60} molecule at 719.99952 u. This detection would corroborate the previous detection of C_{60} in meteorites (Becker et al. 1996, 2000). However, we cannot confidently state if fullerene species are natively present in the IOM or if they are generated by the ionization process (Pereira et al. 2014; Santos et al. 2016) during the measurements in our LDI-FT-ICR-MS.

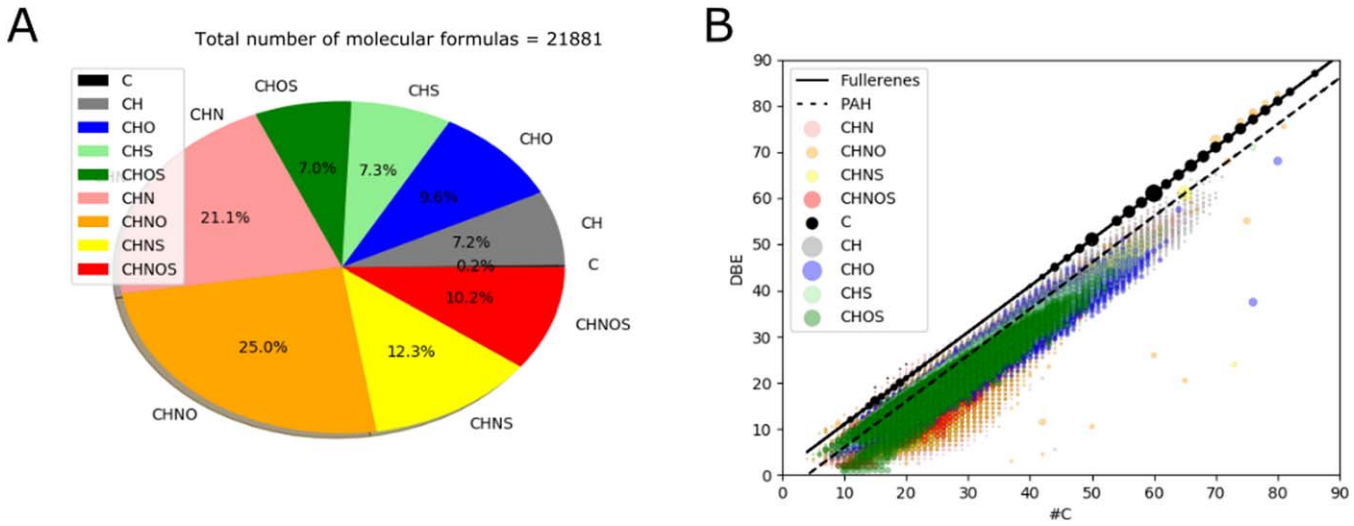

Figure 3. Distribution of the chemical families observed in our Paris IOM with a power laser energy of 13% (A). Double bond equivalent (DBE) as a function of the number of carbon (#C) for the same families (B). Slopes of pure PAHs and pure carbon (fullerenes) structures are also reported for references.

The higher sensitivity in the fullerene detection at 20% laser power tends to promote degradation and fragmentation of the native molecules, resulting in a higher detection of fullerenes (Appendix A.2). Nevertheless, this process demonstrates that IOM also contains the carbon structures that could be related to rather large PAH molecules, even if molecular ions detected at a higher laser power could come from recombination (Wu et al. 2013; Aubriet et al. 2018).

3.3. Insights Into Molecular Structures

To obtain information about the structures of molecules released from the IOM, CID experiments were performed on some selected precursor ions. For condensed aromatic structures, two structural models exist concerning the cores of such compounds: (i) aromatic cores linked by aliphatic bridges (archipelago type), and (ii) a single large aromatic core with several aliphatic carbon ramifications (island type). Each model has a typical fragmentation pattern in CID experiments (Chacón-Patiño et al. 2017, 2018a, 2018b; Le Maître et al. 2019). In the present case, we will focus on hydrocarbon molecules (C_xH_y) and mono-nitrogen compounds ($C_xH_yN_1$) at the m/z 270 nominal mass (a second example at m/z 306 is also reported in the Supporting Information showing the same type of characteristic fragmentation, Figure A10).

The C_xH_y molecular ions (Figure 4, 1) are radical cations. Regarding the DBE versus #C plots, many fragments are observed following the PAH line (red line). In Figure 4, from the m/z 270.140 ($C_{21}H_{18}^{+\bullet}$) precursor ion, the most intense detected fragment ions series is produced through losses of alkyl radicals ($C_nH_{2n+2}^{\bullet}$) (Figure A11, 20 eV). The corresponding bar plot, displaying this ion series, shows a major fragment at #C = 17 when the collision energy is increased (Figure A11; 30, 40, and 50 eV). Thus, this fragment ion should be a fully de-alkylated aromatic core. As the precursor ion is a cationic radical, the main fragmentation scheme involves losses of alkyl radical groups. As there is mainly no loss of DBE during fragmentation, this compound should be an island-type structure (Chacón-Patiño et al. 2018b). Among the many possible isomers, a hypothetical formula of the molecule and its corresponding fragmentation pattern are given in Figure 4, (1), and Figure A12(A). The large number of fragments indicates a high number of isomers for each precursor ion (Ruf et al. 2019).

The second (Figure 4, (2)) and third examples (Figure 4, (3)) focus on species containing one nitrogen atom ($C_xH_yN_1$) in their molecular formula. Because these represent protonated molecules $[M+H]^+$, we assume that they present a basic pyridine-type core (Figures A12(B) and (C)). Pyridine-type cores are privileged over pyrrole-type cores because they are detected in positive mode, while pyrroles are detected in negative mode. Considering island-type molecules, losses of small alkanes (C_nH_{2n+2}), with fragment ions keeping the nitrogen atoms, are mainly observed (Le Maître et al. 2019). It is therefore possible to recover the specific ions from this precursor by extracting ion series containing one nitrogen atom. Two isobaric $C_xH_yN_1$ species were fragmented, one in zone 1 and the other in zone 2 of the DBE/#C (Figure 2(A)). From the protonated precursors, it id mainly losses of alkane molecules that are detected. Both molecules are fitted with the island model regarding the DBE plots and bar plots. However, the ones in zone 2 have a different fragmentation pattern (Figure A12(C)) as the de-alkylation process is more pronounced. It means that this molecule presents a higher alkylation than in zone 1. This effect is only observed for N-bearing molecules.

These CID experiments demonstrate that hydrocarbon species (C_xH_y) and nitrogenated ones ($C_xH_yN_1$, zone 1) follow mainly a low-alkylated island structural pattern whereas some other nitrogenated species have a highly alkylated island pattern ($C_xH_yN_1$, zone 2; Figure A10). The nitrogen-containing molecules bear either highly aromatic compartments with a low degree of branching (zone 1) or compartments presenting a high number of ramifications (zone 2). Fragmentation patterns of $C_xH_yO_1$ and $C_xH_yS_1$ families are also reported in supporting information. These two other families seem to correspond to low-alkylated island-type molecules (PAH-like structures), bearing their heteroatoms (O and S) in the aromatic cores of their structures (Figure A13).

4. Discussion

Based on comprehensive analyses, chondritic IOM is generally considered to be cross-linked macromolecular structures, including heteroatoms, distributed either in aromatic units or in the

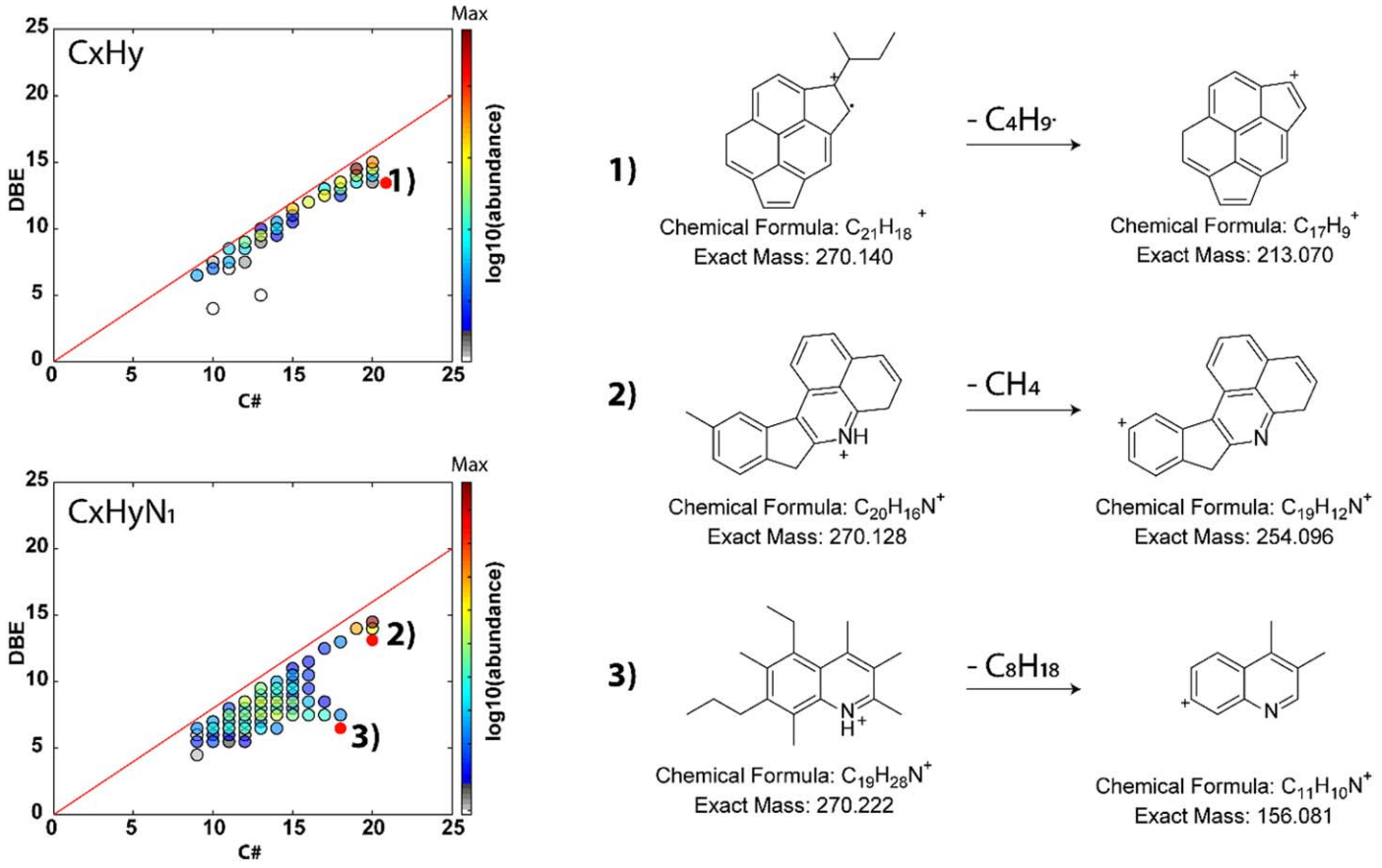

Figure 4. CID fragmentation experiments for the Paris IOM, laser energy of 25%. DBE vs. C# plots of the CH family CID energies at 40 eV of m/z 270, or DBE vs. #C maps of the CHN_1 families with CID fragmentation at 40 eV of m/z 270. Example of formulas of the molecule and its corresponding fragmentation pattern are also reported.

aliphatic chains (Derenne & Robert 2010). This investigation of the Paris meteorite shows that a fraction of molecules with low masses is part of this IOM. Indeed, even if we cannot exclude that some molecular ion detected could share covalent bonds with the macromolecular structure (see method section), the low laser energy used shows that part of the Paris IOM is made up of small units with masses ranging from 100 to 700 u. In addition, significant molecular diversity is also present with various molecular series ranging from CH to CHNOS molecules. These molecules are mainly condensed aromatic structures with aliphatic substituents. Furthermore, heteroatoms are instead included in aromatic rings rather than in aliphatic chains owing to the observed fragmentation patterns. Elemental atomic ratios of this distribution (Table 1) give values ($H/C = 0.81$, $N/C = 0.07$, $O/C = 0.07$ and $S/C = 0.04$) near the ones observed from previous bulk elemental analysis of Paris IOM ($H/C = 0.71$, $N/C = 0.04$, $S/C = 0.09$; Vinogradoff et al. 2017). We observe that this fraction of the Paris IOM presents a lower O/C ratio and a higher aliphatic/aromatic ratio than other IOMs from CMs (Alexander et al. 2007). The higher N/C can also be due to the pristine nature of the Paris IOM but we cannot exclude artifacts due to LDI ionization that tends to favor the ionization of PAHs bearing nitrogen functions (Cho et al. 2013). Compared to the soluble organic matter (SOM) analysis of meteorites, the molecules observed by LDI-FT-ICR-MS present an interesting similar molecular diversity (Schmitt-Kopplin et al. 2010, 2012; Hertkorn et al. 2015) However, their aromaticity is much more pronounced ($H/C = 1.55$ for Murchison SOM). Furthermore,

Table 1
For Each Detected Family, Their Number of Attributions and Their Average Molecular Formula are Reported

Average Molecular Formula		Number of Formula Attributions		Chemical Families
11%	13%	11%	13%	
$[C_{58}]^+$	$[C_{40}]^+$	1	45	C
$[C_{33}H_{17}]^+$	$[C_{38}H_{16}]^+$	895	1577	CH
$[C_{29}H_{18}O_2]^+$	$[C_{32}H_{17}O_2]^+$	890	2091	CHO
$[C_{27}H_{14}S]^+$	$[C_{30}H_{14}S_2]^+$	666	1601	CHS
$[C_{25}H_{15}OS]^+$	$[C_{27}H_{16}OS_2]^+$	362	1539	CHOS
$[C_{27}H_{23}N_2]^+$	$[C_{32}H_{19}N_2]^+$	3405	4626	CHN
$[C_{26}H_{25}N_2O_2]^+$	$[C_{28}H_{21}N_2O_2]^+$	4805	5447	CHNO
$[C_{24}H_{19}N_2S]^+$	$[C_{28}H_{16}N_2S]^+$	1754	2693	CHNS
$[C_{24}H_{21}N_2OS]^+$	$[C_{27}H_{17}N_2OS]^+$	1418	2230	CHNOS
$[C_{26}H_{16}N_2OS]^+$	$[C_{30}H_{15}N_2O_2]^+$	8791	16846	Zone 1
$[C_{28}H_{36}N_2O_2S]^+$	$[C_{27}H_{33}N_2O_2S_2]^+$	3362	2220	Zone 2
$[C_{26}H_{23}N_2O_2S]^+$	$[C_{29}H_{19}N_2O_2S]^+$	11404	15018	N species
$[C_{29}H_{16}OS]^+$	$[C_{32}H_{16}O_2S_2]^+$	2827	6863	Non-N species
$[C_{14}H_{25}N_2OS]^+$	$[C_{12}H_{21}N_2OS_2]^+$	311	280	Aliphatics
$[C_{17}H_{26}N_2O_2S]^+$	$[C_{14}H_{20}N_2O_2S_2]^+$	982	952	Aromatics
$[C_{28}H_{21}N_2O_2S]^+$	$[C_{31}H_{18}N_2O_2S]^+$	12939	20626	Condensed aromatics
$[C_{27}H_{22}N_2O_2S]^+$	$[C_{30}H_{18}N_2O_2S]^+$	14232	21881	Total

Note. Also reported are the ones for zones 1 and 2 of nitrogen species, the whole nitrogen species, and the non-nitrogen species, as well as the total attributions. Data for 11% and 13% of the laser power are displayed.

O/C is lower than the one observed in Murchison (O/C = 0.2) for instance, while a rather similar N/C is observed (Murchison, N/C = 0.03). These molecules clearly present numerous characteristics with other IOM analyses in terms of aromaticity and heteroatom content, but with a molecular diversity reminiscent of the SOM one.

Among this fraction of the Paris IOM, variations in the degree of aromaticity are also observed, especially in nitrogen-bearing molecules. While non-nitrogen-bearing molecules present a homogeneous aromaticity (H/C = 0.55, O/C = 0.03, S/C = 0.03), nitrogen-bearing species present two distributions (Figure 2): one displaying aromaticity near the non-nitrogen-bearing species (H/C = 0.61, N/C = 0.08, O/C = 0.04, S/C = 0.04), and the other presenting a much lower aromaticity (H/C = 1.28, N/C = 0.07, O/C = 0.07, S/C = 0.04). The structure of this low aromaticity distribution is quite different, presenting molecules with smaller aromatic cores while increasing aliphatic branching (Figure 4). This observation tends to show that nitrogen could have taken an important role in the chemical reactivity that led to the formation of these nitrogen-bearing species or that at least two sets of precursors would exist. In addition to these low mass distributions, the presence of condensed aromatic structures is observed up to the detection of fullerenes that are pure carbon structures. The presence of fullerenes was already observed with other analytical techniques (Becker et al. 1996, 2000; Berné et al. 2015). These observations indicate that carbonaceous materials (PAH or hydrogen amorphous carbon (HAC)) are present in the Paris IOM, which could explain the detection of the low-mass molecules. Indeed, one plausible interpretation would be that low-mass molecules are probably trapped in large PAH units by noncovalent hydrophobic interactions, explaining that they are difficult to extract with classical solvents, and remain associated with the IOM. This is specially the case for molecules detected at low laser power (11%). The laser enables desorbing these low-mass molecules and then, by increasing the laser power (13%–20%), higher structures can be desorbed and thus observed. However, at these higher energies (13%, 20%), a fraction of molecules that were attached to the PAH/HAC structures by covalent bonds could also be released; their amount is still difficult to evaluate. In addition, the treatment allowing the isolation of the IOM from the Paris meteorite, and particularly the acidic hydrolysis, could break some labile acidic chemical functions (Alexander et al. 2017), releasing these small molecular units that can then be hydrophobically adsorbed on aromatic structures.

A complete understanding of mechanisms at the origin of these low-mass molecular fractions is currently difficult to apprehend. Different scenarios are generally suggested to explain the IOM formation: an origin from ISM precursors or during the solar nebula evolution (Alexander et al. 2017). Concerning the fraction analyzed here, with the high molecular diversity that recalls the one observed for the SOM of the Murchison meteorite (Schmitt-Kopplin et al. 2010), one can suggest that they originate from the processing of dense molecular ices during the protosolar nebula evolution phase (Caselli & Ceccarelli 2012; Tartèse et al. 2018). There is evidence that amino acid are related between laboratory ice analogs and meteorites (Modica et al. 2018). The chemistry that drives the molecular formation in these environments is mainly related to the radical chemistry that occurs at low temperatures followed by an efficient thermal reactivity in the solid phase of the evaporating ices (Fresneau et al. 2017). Indeed, despite such an apparently simple process, a high diversity of molecules is observed in such astrophysical ice analogs (thousands of molecules with masses up to 4.000 Da; Danger et al. 2013). In addition, it was experimentally shown that when soluble organic molecules from ice analogs are submitted to energetic particles in vacuum (UV photons from the young Sun at the edge of the protoplanetary disk), the formation of an insoluble organic material is observed, a material that could well be then incorporated in small bodies of the solar system (de Marcellus et al. 2017). The composition of both of these organic materials is highly impacted by the presence of nitrogen that drives the chemistry to different molecular families (Fresneau et al. 2017), which could explain the two distributions observed on the nitrogen-bearing species of this Paris IOM. This would imply that before accretion, radical chemistry would have driven the reactivity that led to this fraction of IOM, such as observed in ice chemistry experiments. The molecular diversity observed with the LDI analysis of the Paris IOM could hence be related to the one generated during the processing of these ice analogs (Danger et al. 2013, 2016). It was indeed observed that the formation of the insoluble material impacts the composition of the soluble fraction, suggesting that a continuity may exist between soluble and insoluble materials (Fresneau et al. 2017; Gautier et al. 2020). During their energetic alteration, soluble residues lose labile chemical functions, leading to a decrease of their aliphaticity as well as a loss of oxygen and nitrogen (Gautier et al. 2020). This mix of soluble and insoluble organics could then be incorporated inside meteoric parent bodies where they could undergo additional evolution under aqueous alteration conditions (Le Guillou & Brearley 2014; Alexander et al. 2017; Vinogradoff et al. 2018, 2020). First experiments on relevant astrophysical molecules in aqueous alteration conditions have indeed shown that an important reactivity occurs, leading to an important molecular reprocessing of the initial organic matter. This process could have also participated in the formation of the both N-bearing groups observed in this work and drive small hydrophobic molecules to interact with condensed aromatic structures where they could be hydrophobically trapped.

5. Conclusions

The investigation of IOM in carbonaceous matter is a mature subject that has required many different analytical tools and techniques for over 30 yr. The chemical and isotope signatures of the IOM confirm that it has witnessed the physical and chemical evolution of the transition between the ISM to the solar system. LDI-FT-ICR-MS(/MS) provides here a complementary picture of the composition of the IOM in the Paris meteorite. It exhibits a mix of low-mass molecules (100–700 u) presenting high molecular diversity. More than 14,000 attributions relative to these molecules have been determined, a number increasing with the laser relative power output used for desorbing these molecules. These molecules are trapped within the large aromatic units forming the IOM backbone and have witnessed the same events as the main IOM component. The LDI-FT-ICR-MS(/MS) measurements reported here suggest that a portion of the molecular fragments associated with the IOM structure can be related to chemistry that occurred in ice during the transition from the ISM to the protosolar nebula. This is consistent with the conclusions

drawn from the H-isotope composition that interstellar-like processes have influenced the formation of the IOM precursors. The large molecular diversity evidenced by these measurements of the IOM does echo the large molecular diversity evidenced by the FT-ICR investigation of soluble organic compounds in CC; this may call into question an evolutionary continuity between these soluble and insoluble organic fractions in carbonaceous chondrites.

We are grateful to the meteorite collection of the Muséum National d'Histoire Naturelle in Paris for providing the sample of the Paris meteorite.

N.C. and L.R. thank the European Research Council for funding via the ERC projects PrimChem (grant agreement No. 636829) and HYDROMA (grant agreement No. 819587).

This work was supported by the European Regional Development Fund (ERDF) No. HN0001343, the European Union's Horizon 2020 Research Infrastructures program (Grant Agreement 731077), the Région Normandie, and the Laboratoire d'Excellence (LabEx) SynOrg (ANR-11-LABX-0029). Access to a CNRS FTICR research infrastructure (FR3624) is gratefully acknowledged.

G.D., A.R., and L.R. thank the Agence nationale de la recherche (RAHIIA_SSOM, ANR-16-CE29-0015), the Centre National d'Etudes Spatiales from its exobiology program, and the Centre National de la Recherche Française (CNRS, "Physique et Chimie du Milieu Interstellaire" (PCMI) and "Programme National de Planétologie" (PNP) programs) for their financial support.

G.D. designed research. L.R. and V.V. performed Paris IOM isolation. G.D. and J.M. performed LDI-FT-ICR-MS(MS) analyses. G.D., A.R., J.M., and J.H. performed data treatments. G.D. wrote the paper. A.R., J.M., J.H., V.V., P.S.-K., C.A., L.R., N.C., I.S.-A., and L.S.H. contributed to the paper writing.

Appendix

A.1. Blank Sample Measured around the Position of the Paris IOM (Laser Energy of 13%)

Figure A1 displays spectrum obtained for a blank sample. It was measured around the position of the Paris IOM (laser energy of 13%) with the same analytical conditions as in Section 3.2. At this position, signals related to the Paris IOM are not observed, which demostrates that features observed in Figure 1 correspond to the Paris IOM and not to contaminations.

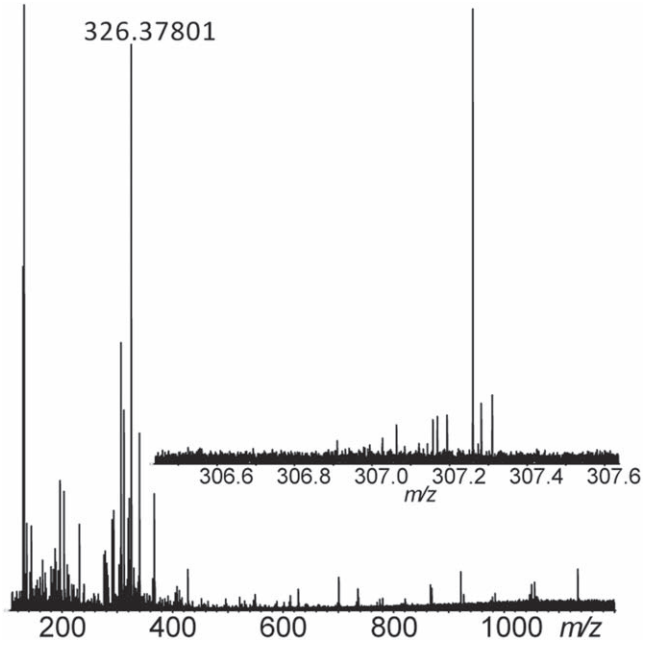

Figure A1. Blank sample measured around the position of the Paris IOM (laser energy of 13%) with the same analytical conditions as in Section 3.2. No signals related to the Paris IOM are observed.

A.2. Influence of Laser Energy

The laser power was initially tested to obtain a repeatable LDI-FT-ICR mass spectrum with a good S/N. Thus, laser powers of 11% and 13%, as well as 20%, were tested. The corresponding mass spectra are given in Figure A1 in which it is shown that an increase of the laser power is responsible for a shift of the mass distribution toward higher m/z values and an increase of the signals relative to fullerene molecular series increase, especially at 20%. It is well known that over a certain threshold, the LDI process is responsible for fragmentation and recombination reactions (Zhigilei & Garrison 1999). In addition, among the artifacts produced by laser, the presence of fullerenes in the mass spectra acquired at laser powers of 13% and 20% has to be interpreted with caution (Santos et al. 2016).

The composition description achieved from the different analyses is given in Figure A2. At laser powers of 11% and 13%, the relative abundances of the different heteroatom classes are close but a higher number of features is obtained at a laser power of 13%. Deeper insight into the data was obtained by means of van Krevelen diagrams and a H/C versus m/z graph (Figure A3). The van Krevelen diagrams of the data obtained at a laser power of 20% show that most of the features are poorly or not oxygenated (low O/C) and highly unsaturated (low H/C), whereas those achieved at the two other laser powers demonstrate species with higher H/C and O/C values. Thus, most of the species ionized with the highest laser powers are certainly artifacts. Comparison of the graphs H/C versus m/z obtained at laser powers 11% and 13% gives evidence that higher-mass compounds for all classes are ionized with higher laser power. In addition, new unsaturated species ($H/C < 0.2$) are observed whereas at laser power 11%, some low-unsaturated components ($1.75 < H/C < 2$) are exclusively observed. Such a behavior was also observed by Aubriet et al. (2018). Therefore, to avoid any misinterpretation of the sample due to laser artifacts, the data interpretation performed from the mass spectrum acquired with a laser power of 11% will be considered.

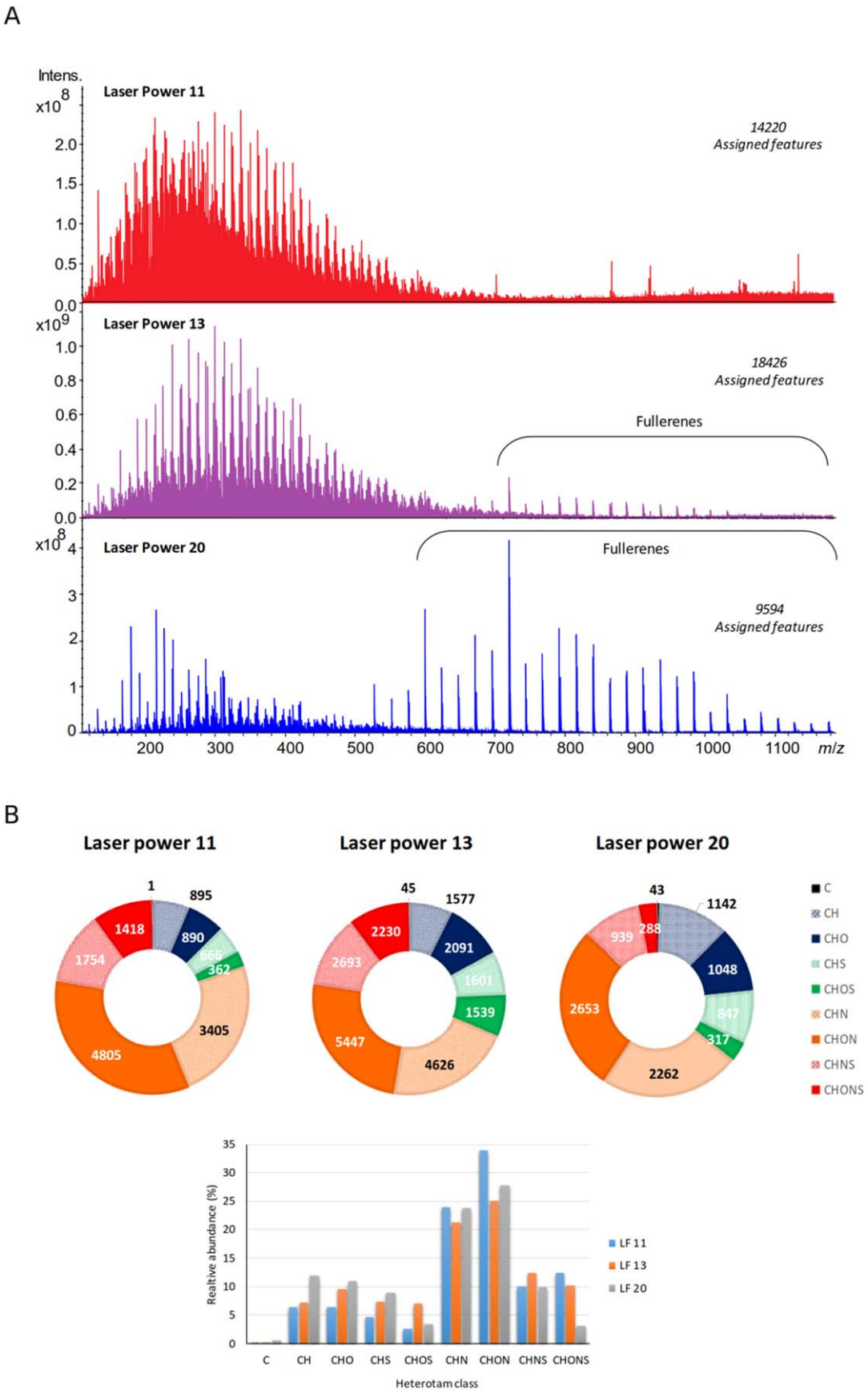

Figure A2. (A) (+) LDI-FT-ICR mass spectra of the IOM from the Paris meteorite acquired with the laser powers of 11%, 13%, and 20%, with the clear increase of the signal intensity relative to the fullerene molecular series highlighted. (B) (Top) Pie charts representing the heteroatom class distribution with the feature numbers, achieved from the (+) LDI-FT-ICR-MS analysis of the IOM of the Paris meteorite with laser powers of 11%, 13%, and 20%. (Bottom) Relative abundances of the different molecular series according to the laser power used.

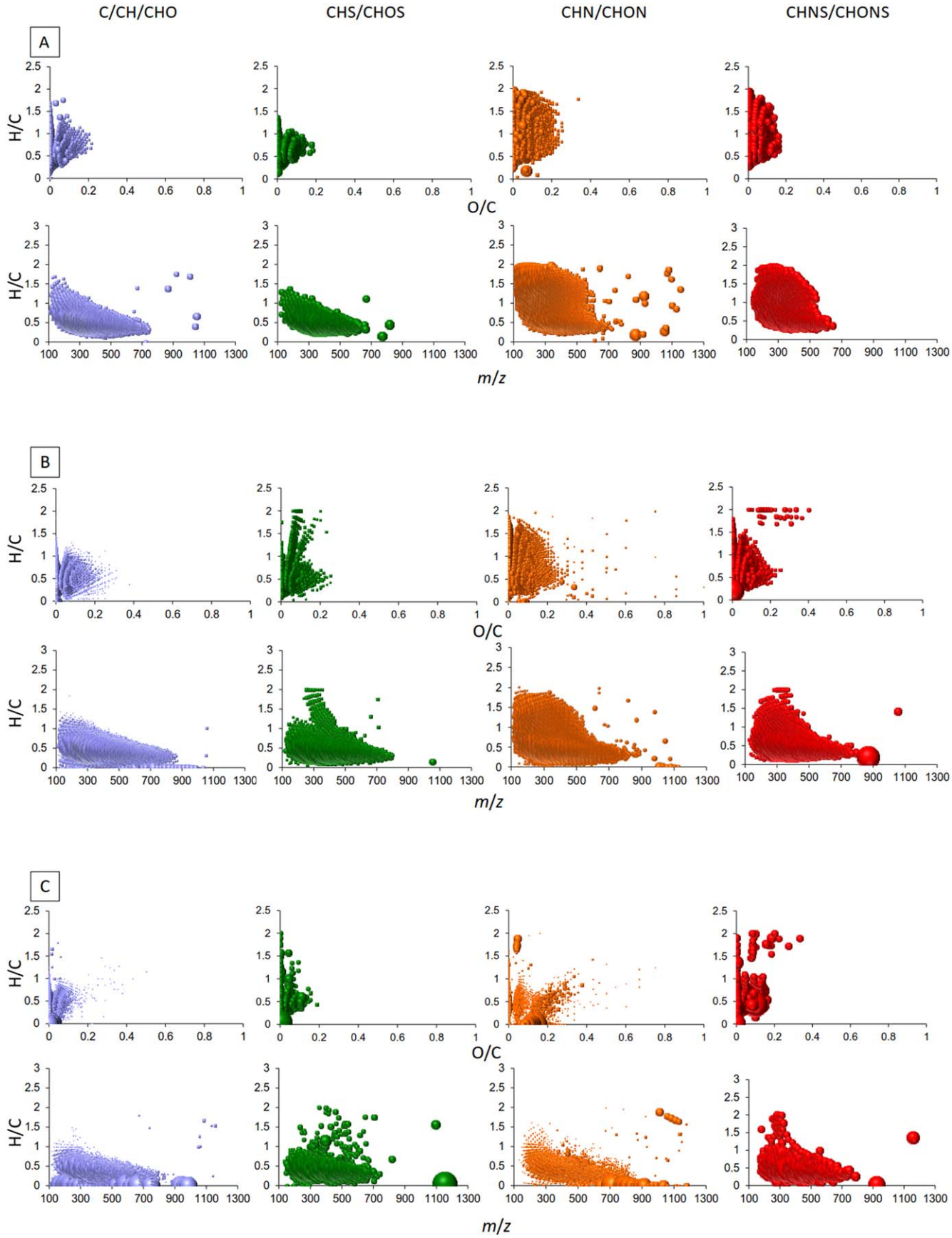

Figure A3. H/C vs. O/C van Krevelen diagrams and H/C vs. m/z graphs achieved for different heteroatom classes obtained from the (+) LDI-FT-ICR-MS analysis of the IOM of the Paris meteorite at laser powers of (A) 11%, (B) 13%, and (C) 20%.

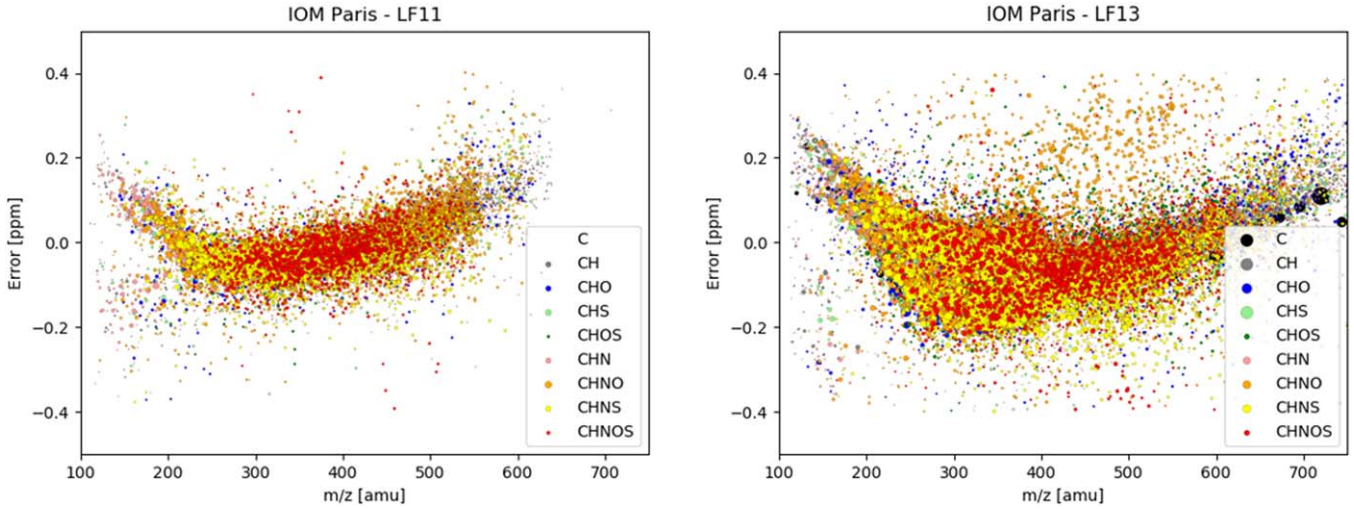

Figure A4. Error plots related to attributions obtained for analyses performed with a laser power of 11% or 13%.

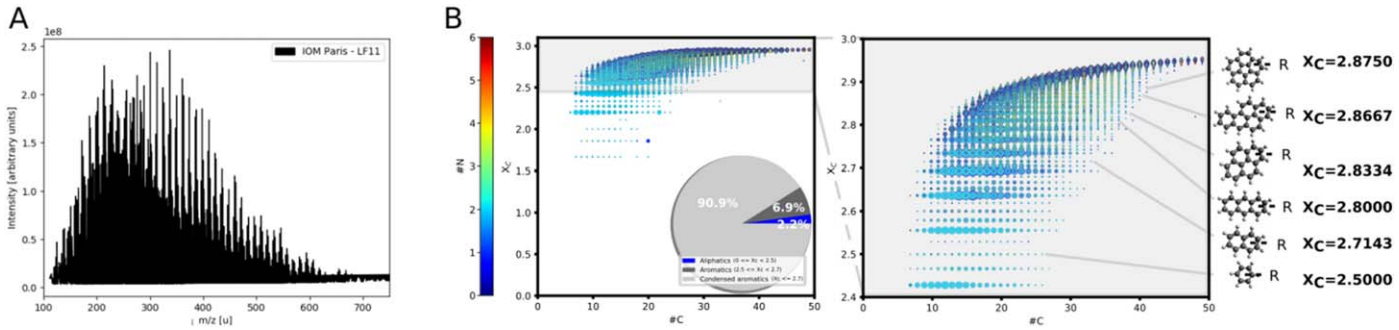

Figure A5. LDI-FT-ICR mass spectrum (laser power at 11%) of the Paris IOM (A) and the X_c distribution of all assigned molecular formulas (B). X_c allows the degree of unsaturation of carbon atoms on each molecule to be estimated. It gives an insight on aromaticity of a molecular skeleton.

A.3. Error Plots Related to Attributions

Figure A4 displays error plots related to attributions obtained for analyses performed with a laser power of 11% or 13%. The profile observed is coherent with the error evolution usually observed with FT-ICR-MS technologies. Attributions can thus be confidently used.

A.4. X_c Distribution of Molecular Formulas

Figure A5 displays LDI-FT-ICR mass spectrum (laser power at 11%) of the Paris IOM (A) and the X_c distribution of all assigned molecular formulas (B). X_c allows the degree of unsaturation of carbon atoms on each molecule to be estimated. It gives an insight on aromaticity of a molecular skeleton. As observed, a large part of detected molecules present a high aromaticity.

A.5. Characteristic of Non-N-bearing and N-bearing Species

Figure A6 displays mass spectra representing the separated distributions of nitrogen and non-nitrogen species (Figure 1(A)), where each family is represented by a different color (A). Repartition of the degree of aromaticity (condensed aromatic, aromatic, or aliphatic) based on X_c values are also given showing that N bearing species are less aromatics than non-N bearing species (B). The number of atoms relative to the number of carbon atoms is also presented for nitrogen and non-nitrogen distributions confirming that N bearing species are less aromatics since the number of H versus C is higher than for non-N bearing species (C).

Figure A7 displays the DBE versus #C representation for both distributions (zone 1 and zone 2) as defined in Figure 2(A). It also presents the relative number of atoms to carbon. The overall shows that zone 1 includes species with a higher aromaticity than zone 2 since the number of H in zone is higher than the one observed in zone 1. Zone 1 presents similarities with non-N bearing species.

A.6. Detailed Data Relative to 13% Laser Power

Figure A8 displays the LDI-FT-ICR mass spectrum of the Paris IOM obtained with a laser energy of 13%. This spectrum allows us to show the molecular diversity that is observed as well as the detection of fullerene, which are not observed with a laser energy of 11%. Figure A9 presents the aromaticity distributions regarding non-N bearing species, the whole N bearing species as well as for their zones 1 and 2.

A.7. Fragmentation Patterns of Studied Ions

Figure A10 displays CID fragmentation experiments for for the Paris IOM with a laser energy of 25%. DBE versus C# plots of the CH families or of the CHN1 families are reported with CID energies at 40 eV of *m/z* 306 showing the number of ions generated. Figure A11 displays bar charts presenting the different fragments (#C) that are generated during the CID at different energies for molecular ions identified in Figures A10. This

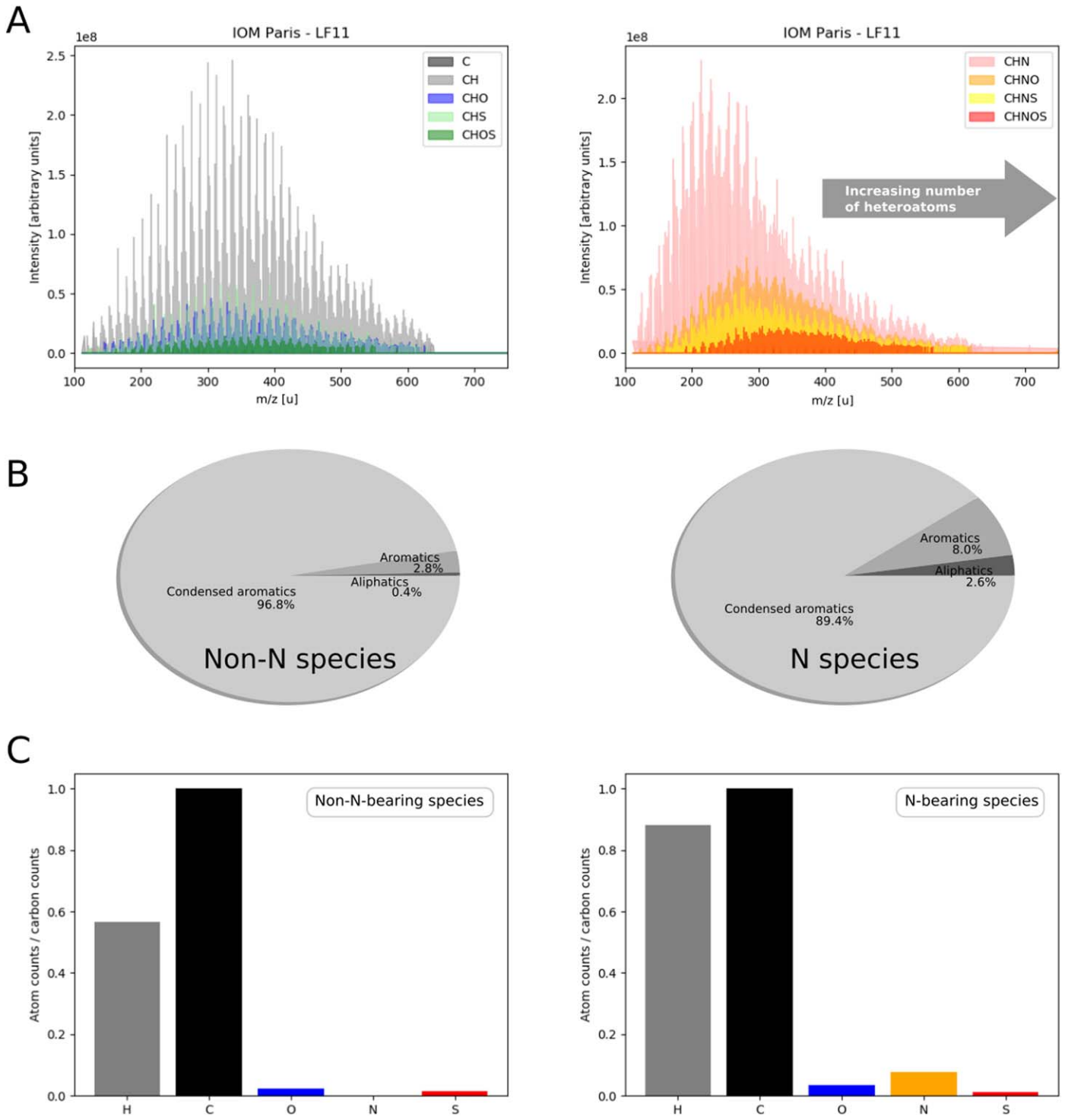

Figure A6. Mass spectra representing the separated distributions of nitrogen and non-nitrogen species (Figure 1(A)), where each family is represented by a different color (A). Repartition of the degree of aromaticity (condensed aromatic, aromatic, or aliphatic) based on X_c values (B). The number of atoms relative to the number of carbon atoms is also presented for nitrogen and non-nitrogen distributions (C).

Figure A11 also reports the stoichiometric formula for some fragments. Figure A12 displays the fragmentation of the ion isolate and shown in Figure 4. The monitoring of the different fragments allows us to determine that nitrogen is inside the aromatic core and that the parent structure is branched with aliphatics. Figure A13 displays CID fragmentation of CHO1 and CHS1 compounds. Examples are given with ions at *m/z* 272 and 310 for CHO1 and with ions at *m/z* 274 and 312 for CHS1. These fragmentation patterns show that heteroatoms are incorporated into the core of the structures.

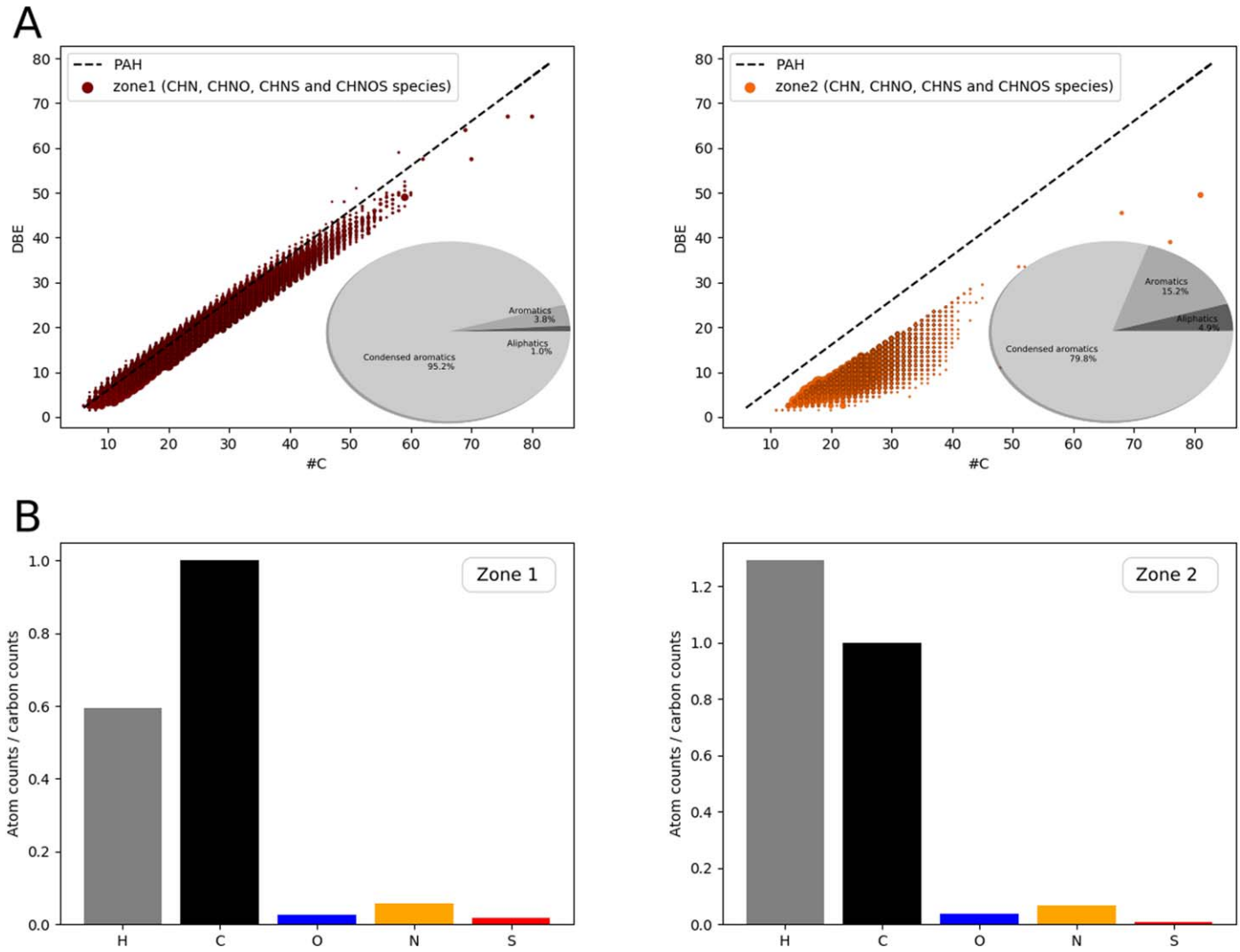

Figure A7. (A) DBE vs. #C representation for both distributions (zone 1 and zone 2) as defined in Figure 2(A). (B) Relative number of atoms to carbon.

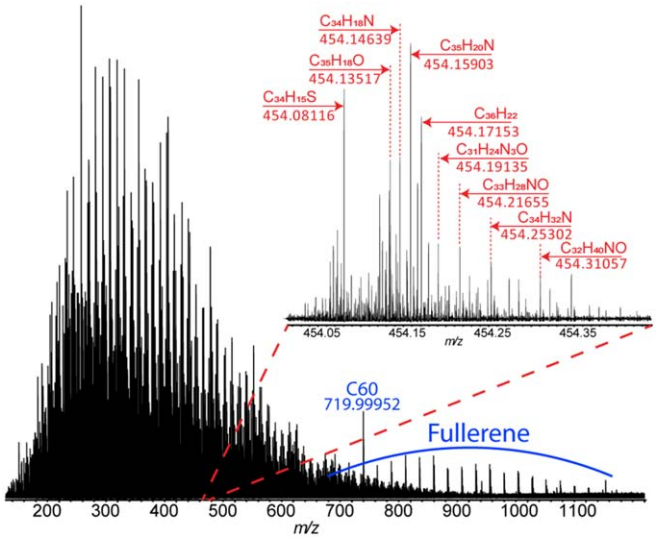

Figure A8. LDI-FT-ICR mass spectrum obtained at a laser energy of 13% of the Paris IOM.

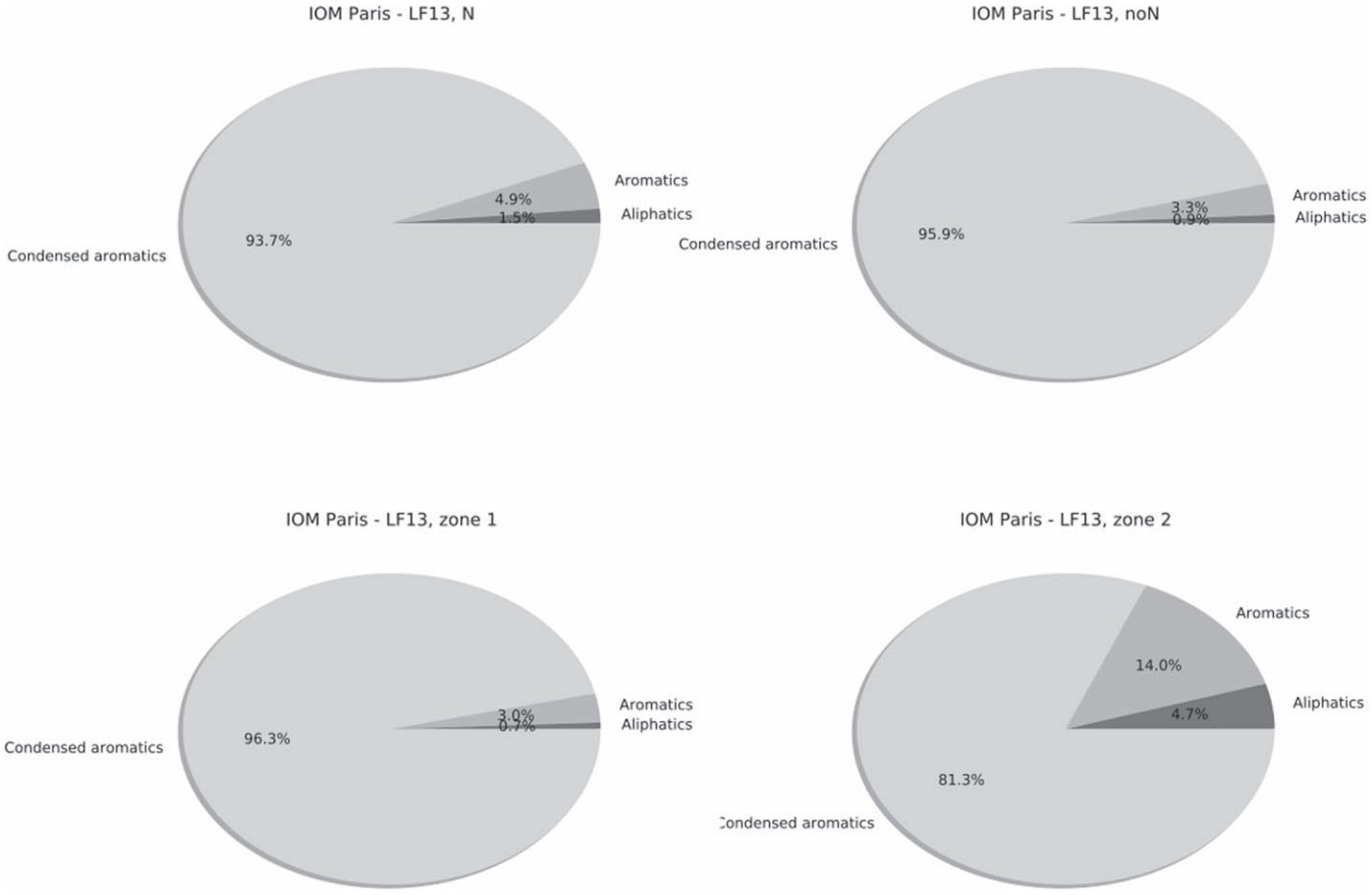

Figure A9. Repartition of the degree of aromaticity (condensed aromatic, aromatic, or aliphatic) based on X_c values for nitrogen-bearing families and non-nitrogen-bearing families, zone 1 and zone 2.

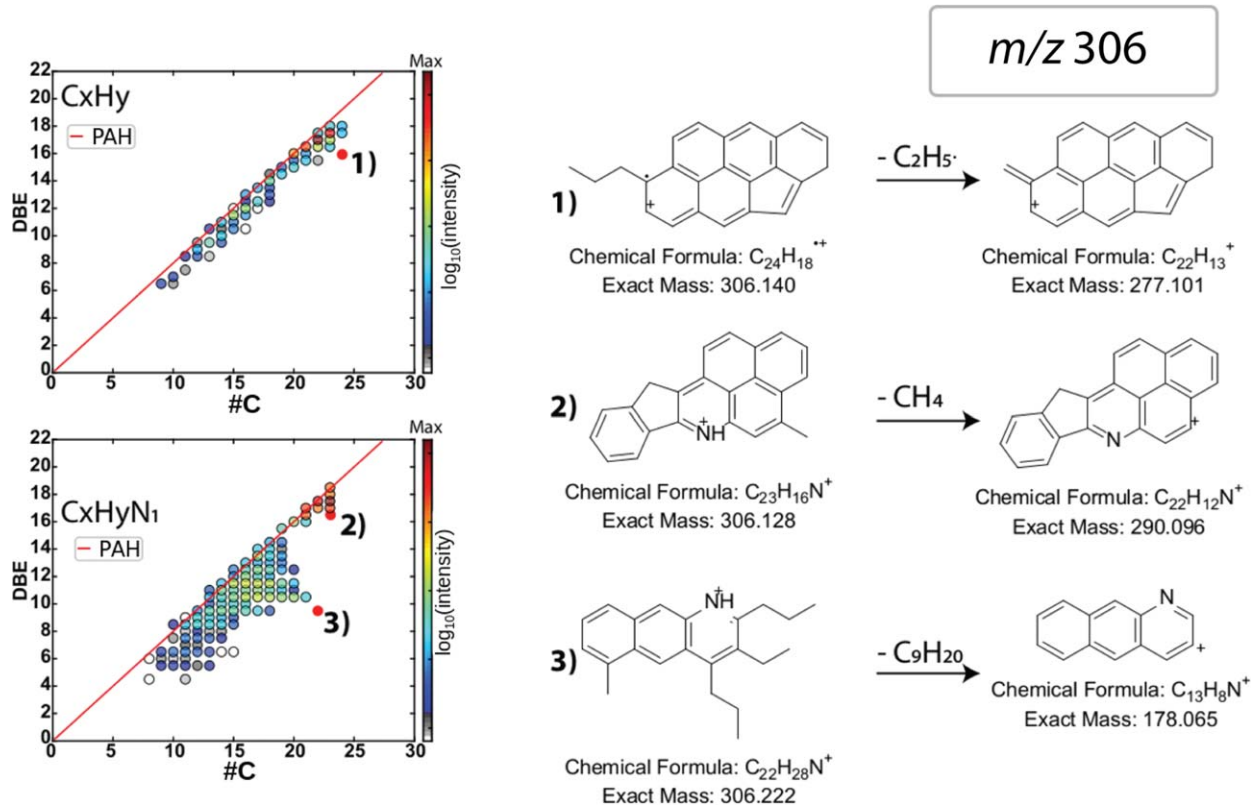

Figure A10. CID fragmentation experiments for for the Paris IOM, laser energy of 25%. DBE vs. C# plots of the CH families CID energies at 40 eV of m/z 306. DBE vs. #C maps of the CHN_1 families with CID fragmentation at 40 eV of m/z 306.

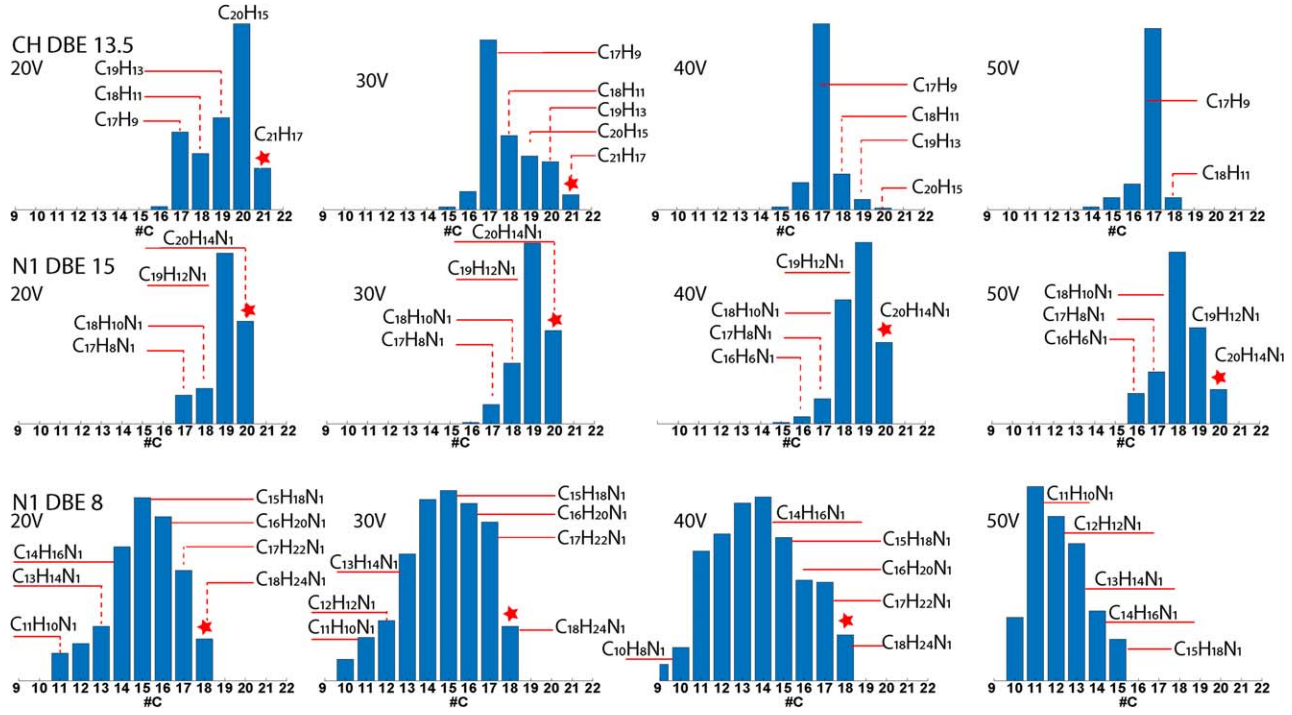

Figure A11. Bart charts presenting the different fragments (#C) that are generated during the CID at different energies for molecular ions identified in Figures A10(A), (B), and (C). Also reports the stoichiometric formula for some fragments.

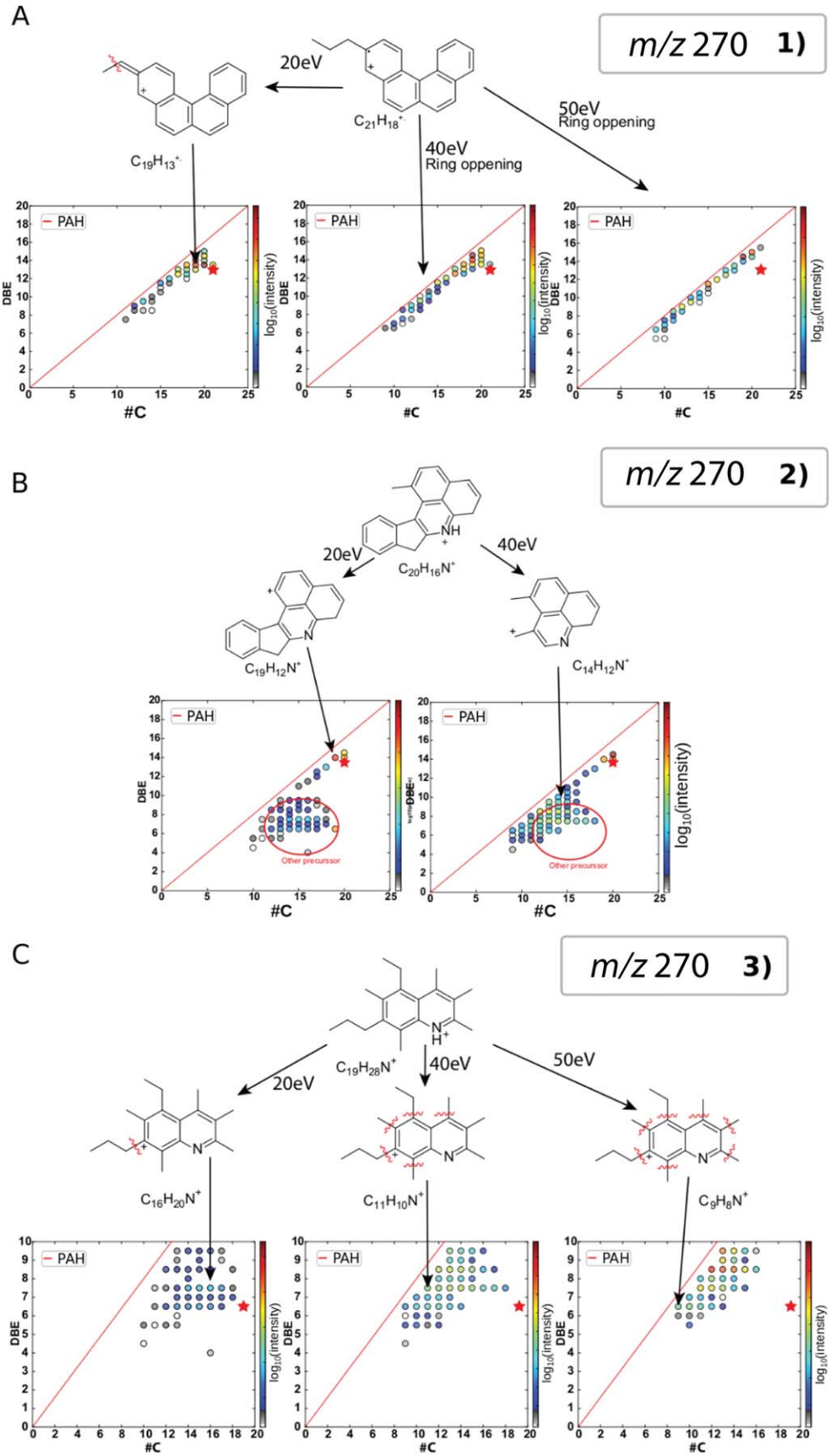

Figure A12. Scheme representing the fragmentation of the ion isolate and shown in Figure 4. Monitoring the different fragments allows us to determine that nitrogen is inside the aromatic core and that the parent structure is branched with aliphatics.

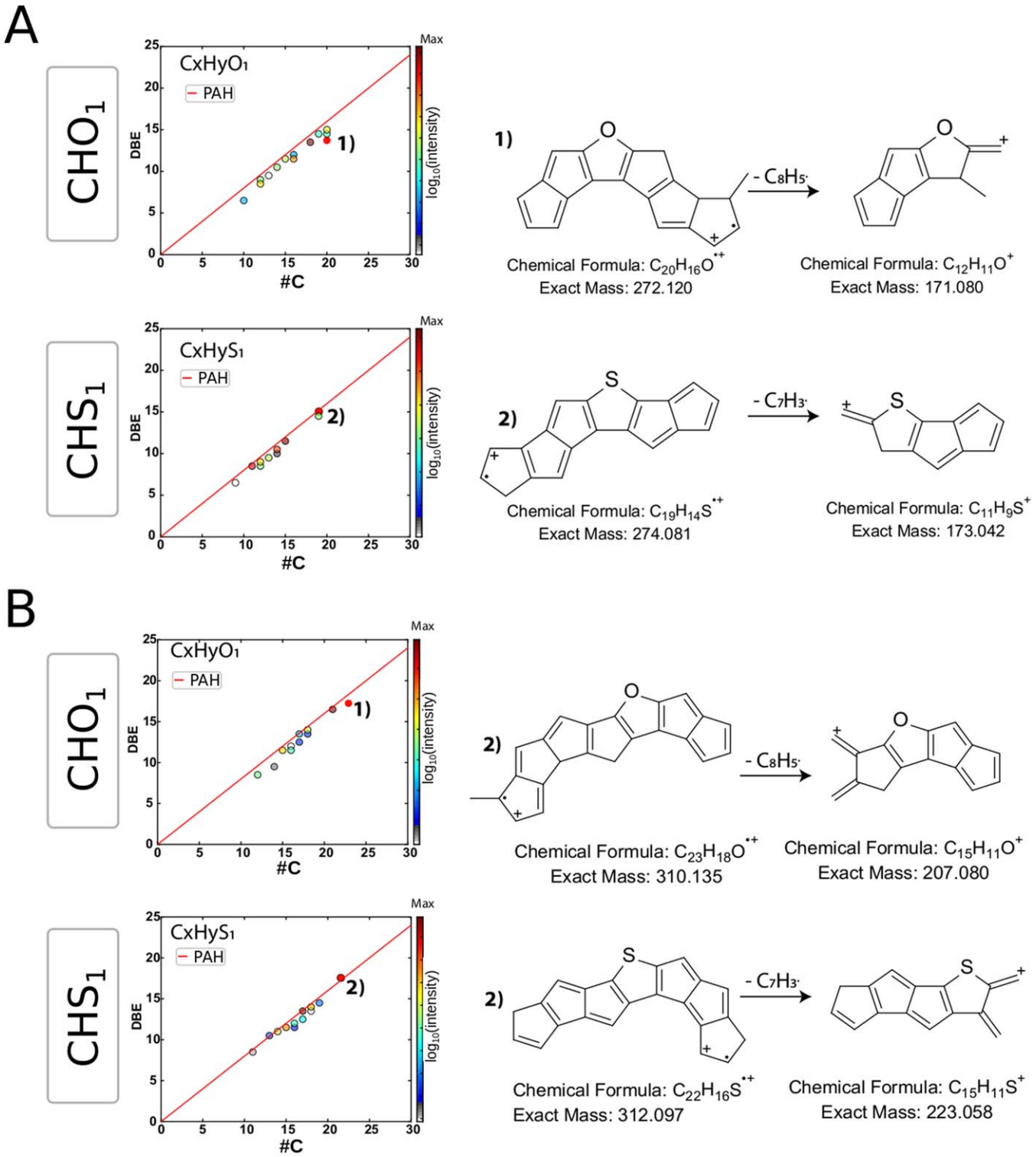

Figure A13. CID fragmentation of CHO1 and CHS1 compounds. (A) Example of m/z 272 and 274, respectively. (B) Example of m/z 310 and 312, respectively. Heteroatoms are incorporated into the core of the structures.

ORCID iDs

Grégoire Danger https://orcid.org/0000-0002-5689-0853
Vassilissa Vinogradoff https://orcid.org/0000-0003-4107-0980
Nathalie Carrasco https://orcid.org/0000-0002-0596-6336

References

Alexander, C. M. O., Cody, G. D., De Gregorio, B. T., Nittler, L. R., & Stroud, R. M. 2017, ChEG, 77, 227
Alexander, C. M. O., Fogel, M. L., Yabuta, H., & Cody, G. D. 2007, GeCoA, 71, 4380

Aubriet, F., Ghislain, T., Hertzog, J., et al. 2018, JASMS, 29, 1951
Barrère, C., Hubert-Roux, M., Lange, C. M., et al. 2012, RCMS, 26, 1347
Becker, L., Poreda, R. J., & Bada, J. L. 1996, Sci, 272, 249
Becker, L., Poreda, R. J., & Bunch, T. E. 2000, PNAS, 97, 2979
Berné, O., Montillaud, J., & Joblin, C. 2015, A&A, 577, A133
Caselli, P., & Ceccarelli, C. 2012, A&ARv, 20, 56
Chacón-Patiño, M. L., Rowland, S. M., & Rodgers, R. P. 2017, Energy & Fuels, 31, 13509
Chacón-Patiño, M. L., Rowland, S. M., & Rodgers, R. P. 2018a, Energy & Fuels, 32, 9106
Chacón-Patiño, M. L., Rowland, S. M., & Rodgers, R. P. 2018b, Energy & Fuels, 32, 314
Cho, Y., Jin, J. M., Witt, M., et al. 2013, Energy & Fuels, 27, 1830
Cody, G. D., & Alexander, C. M. O. 2005, GeCoA, 69, 1085
Cody, G. D., Alexander, C. M. O., & Tera, F. 2002, GeCoA, 66, 1851
Cody, G. D., Heying, E., Alexander, C. M. O., et al. 2011, PNAS, 108, 19171
Danger, G., Fresneau, A., Abou Mrad, N., et al. 2016, GeCoA, 189, 184
Danger, G., Orthous-Daunay, F., de Marcellus, P., et al. 2013, GeCoA, 118, 184
de Marcellus, P., Fresneau, A., Brunetto, R., et al. 2017, MNRAS, 464, 114
Derenne, S., & Robert, F. 2010, M&PS, 45, 1461
Fresneau, A., Mrad, N. A., LS d'Hendecourt, L., et al. 2017, ApJ, 837, 168
Gardinier, A., Derenne, S., Robert, F., et al. 2000, E&PSL, 184, 9
Gautier, T., Danger, G., Mousis, O., et al. 2020, E&PSL, 531, 116011
Göpel, C., Birck, J.-L., Galy, A., Barrat, J.-A., & Zanda, B. 2015, GeCoA, 156, 1
Hayatsu, R., Matsuoka, S., Scott, R. G., Studier, M. H., & Anders, E. 1977, GeCoA, 41, 1325
Hertkorn, N., Harir, M., & Schmitt-Kopplin, P. 2015, Magn. Reson. Chem., 53, 754
Hewins, R. H., Bourot-Denise, M., Zanda, B., et al. 2014, GeCoA, 124, 190
Kanawati, B., Bader, T. M., Wanczek, K.-P., Li, Y., & Schmitt-Kopplin, P. 2017, RCMS, 31, 1607
Le Guillou, C., & Brearley, A. 2014, GeCoA, 131, 344
Le Maître, J., Hubert-Roux, M., Paupy, B., et al. 2019, FaDi, 218, 417
Leroux, H., Cuvillier, P., Zanda, B., & Hewins, R. H. 2015, GeCoA, 170, 247
Maillard, J., Carrasco, N., Schmitz-Afonso, I., Gautier, T., & Afonso, C. 2018, E&PSL, 495, 185
Marrocchi, Y., Gounelle, M., Blanchard, I., Caste, F., & Kearsley, A. T. 2014, M&PS, 49, 1232
Modica, P., Martins, Z., Meinert, C., Zanda, B., & d'Hendecourt, L. L. S. 2018, ApJ, 865, 41
Orthous-Daunay, F.-R., Quirico, E., Lemelle, L., et al. 2010, E&PSL, 300, 321
Orthous-Daunay, F.-R.-R., Quirico, E., Beck, P., et al. 2013, Icar, 223, 534
Pearson, V. K., Sephton, M. A., Franchi, I. A., Gibson, J. M., & Gilmour, I. 2006, M&PS, 41, 1899
Pereira, T. M. C., Vanini, G., Tose, L. V., et al. 2014, Fuel, 131, 49
Pizzarello, S., Cooper, G. W., & Flynn, G. J. 2006, in Meteorites and the Early Solar System II, ed. D. S. Lauretta & H. Y. McSween, Jr. (Tucson, AZ: Univ. Arizona Press), 625
Qi, Y., Witt, M., Jertz, R., et al. 2012, RCMS, 26, 2021
Remusat, L. 2015, in Planetary Mineralogy, ed. M. R. Lee & H. Leroux (Jena: The Euro. Mineral. Union), 33, http://www.minsocam.org/msa/EMU_Notes/EMU015.html
Remusat, L., Derenne, S., & Robert, F. 2005a, GeCoA, 69, 4377
Remusat, L., Derenne, S., Robert, F., & Knicker, H. 2005b, GeCoA, 69, 3919
Remusat, L., Guan, Y., Wang, Y., & Eiler, J. M. 2010, ApJ, 713, 1048
Remusat, L., Guillou, C., Rouzaud, J.-N., et al. 2008, M&PS, 43, 1099
Rubin, A. E., Trigo-Rodríguez, J. M., Huber, H., & Wasson, J. T. 2007, GeCoA, 71, 2361
Ruf, A., D'Hendecourt, L., & Schmitt-Kopplin, P. 2018, Life, 8, 18
Ruf, A., Poinot, P., Geffroy, C., D'Hendecourt, L. L. S., & Danger, G. 2019, Life, 9, 1
Santos, V. G., Fasciotti, M., Pudenzi, M. A., et al. 2016, Analyst, 141, 2767
Schmitt-Kopplin, P., Gabelica, Z., Gougeon, R. D., et al. 2010, PNAS, 107, 2763
Schmitt-Kopplin, P., Herir, M., Kanawati, B., et al. 2012, Metit, 2, 79, http://www.meteorites.pwr.wroc.pl/issues/2/schmitt-koplin_et_al.pdf
Sephton, M. A. 2002, Nat. Prod. Rep., 19, 292
Tartèse, R., Chaussidon, M., Gurenko, A., Delarue, F., & Robert, F. 2018, PNAS, 115, 8535
Vinogradoff, V., Bernard, S., Le Guillou, C., & Remusat, L. 2018, Icar, 305, 358
Vinogradoff, V., Le Guillou, C., Bernard, S., et al. 2017, GeCoA, 212, 234
Vinogradoff, V., Le Guillou, C., Bernard, S., et al. 2020, GeCoA, 269, 150
Wang, N., Zhi, Y., Wei, Y., et al. 2020, NatCo, 11, 1079
Wu, Q., Pomerantz, A. E., Mullins, O. C., & Zare, R. N. 2013, JASMS, 24, 1116
Yabuta, H., Naraoka, H., Sakanishi, K., & Kawashima, H. 2005, M&PS, 40, 779
Yassine, M. M., Harir, M., Dabek-Zlotorzynska, E., & Schmitt-Kopplin, P. 2014, RCMS, 28, 2445
Zhigilei, L. V., & Garrison, B. J. 1999, ApPhL, 74, 1341